

Supplementary Information

Phenazine anodes for ultralong cycle life aqueous rechargeable batteries

Leilei Li,^{ac} Long Chen,^a Yuehua Wen,^{*a} Tengfei Xiong,^e Hong Xu,^d Wenfeng Zhang,^a Gaoping Cao,^a Yusheng Yang,^a Liqiang Mai,^{*b} and Hao Zhang^{*a}

^a Research Institute of Chemical Defense, Beijing 100191, China

^b State Key Laboratory of Advanced Technology for Materials Synthesis and Processing, Wuhan University of Technology, Wuhan 430070, China.

^c School of Chemical & Environmental Engineering, China University of Mining and Technology-Beijing (CUMTB), Beijing 100083, China.

^d Institute of Nuclear and New Energy Technology, Tsinghua University, Beijing 100084, China.

^e Department of Chemistry, City University of Hong Kong, Kowloon, Hong Kong SAR 999077, P. R. China

*Correspondence :

Prof. Hao Zhang, Email: dr.h.zhang@hotmail.com

Prof. Liqiang Mai, Email: mlq518@whut.edu.cn

Prof. Yuehua Wen, Email: wen_yuehua@126.com

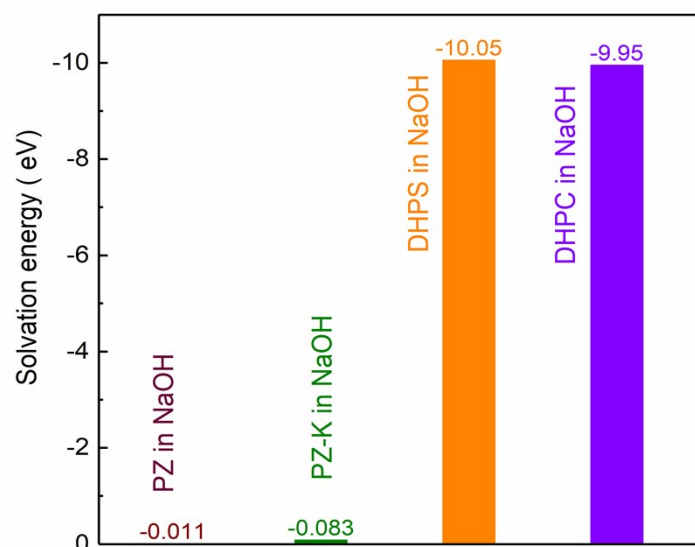


Fig. S1. Solvation Energy of phenazine in water, HCl and its reduced products in the aqueous NaOH solution.

The solubility of an organic molecule can be qualitatively predicted by using DFT calculations of the solvation energy (ΔG_{Sol}), which was the bonding energy difference of the optimized structure under the gas phase and implicit dielectric continuum (COSMO) model.^{1,2 6,7} Smaller value of the solvation energy presents worse solubility. As reported by Hollas et al.,³⁸ phenazine-derivatives of 7, 8-dihydroxyphenazine-2-sulfonic acid (DHPS) and 7,8-dihydroxyphenazine-2-carboxylic acid (DHPC) both delivered the ΔG_{Sol} of ~ 10.0 eV and demonstrated the solubility of 0.95 M and 1.45 M in 1 M NaOH, respectively. As shown in Fig. S1, the solvation energy of phenazine and its reduced products (PZ-K) were much lower than that of DHPS and DHPC, indicating their insolubility in water.

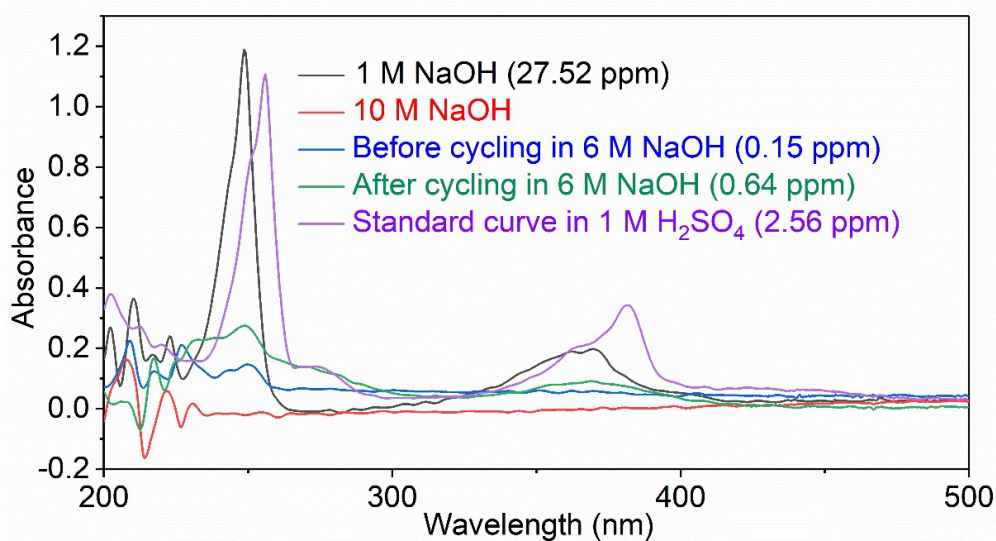


Fig. S2. UV-vis spectra of nPZ/KB anode before and after cycling in NaOH solution.

In order to investigate the solubility of nPZ/KB and its reduced products in alkaline electrolytes, UV-vis spectroscopy technology was carried out to detect the concentrations of nPZ/KB in the 6 M NaOH electrolyte (150 μ L) in the coin cell. As shown in Fig. S2, after the coin cell was stored for one week, only the extremely low concentration (0.15 ppm) of nPZ/KB was detected. In addition, it was also verified that the solubility of phenazine in NaOH solution decreased with the increase of NaOH concentration. In 10 M NaOH solution, the concentration of nPZ/KB was too low to be detected. What's more, in order to explore the solubility of the reduced products of nPZ/KB in the used electrolyte, the stored coin cell was charged/discharged at a pulse current density of 0.15 C for 0.5 h. After the 3 cycles, the detected concentration of phenazine and its reduced products was still very low (0.64 ppm), which verified the insolubility of nPZ/KB's reduced products. Except for the inherent insolubility of nPZ/KB and its reduced products, the obvious π - π adsorption between the nano-phenazine and KB would further inhibit the dissolution of nPZ/KB and its reduced products into the electrolyte (Fig. S12). Therefore, the nPZ/KB could obtain the ultra-long cycle life (100,000 cycles) with the capacity retention (76%).

Table S1. Comparisons of representative anode materials of ARBs.

Entry	Anode	Theoretical capacity (mAh g ⁻¹)	Discharge capacity at 1C (mAh g ⁻¹)	Stability (capacity retention /cycles/current density)	Reference.
1	V ₂ O ₅	/	125	96%/500/5 C	4
2	LiTi ₂ (PO ₄) ₃ /C	138	122	84%/1,000/5 C	5
3	NaTi ₂ (PO ₄) ₃ /C	133	110	95%/3,600/3 C	6
4	PPTO	309	229	80%/3,000/1 C	7
5	PTO	409	395	97%/1,500/2 C	7
6	PAQS	225	200	85%/1,350/1 C	7
7	PNFE	189	135	91.2%/1,000/10 C	8
8	Polyimide	183	160	70%/50,000/55 C	9
9	PNDIE	183	148	81%/4,000/5 C	10
10	PZ	298	304	91%/100,000/100 C	This work

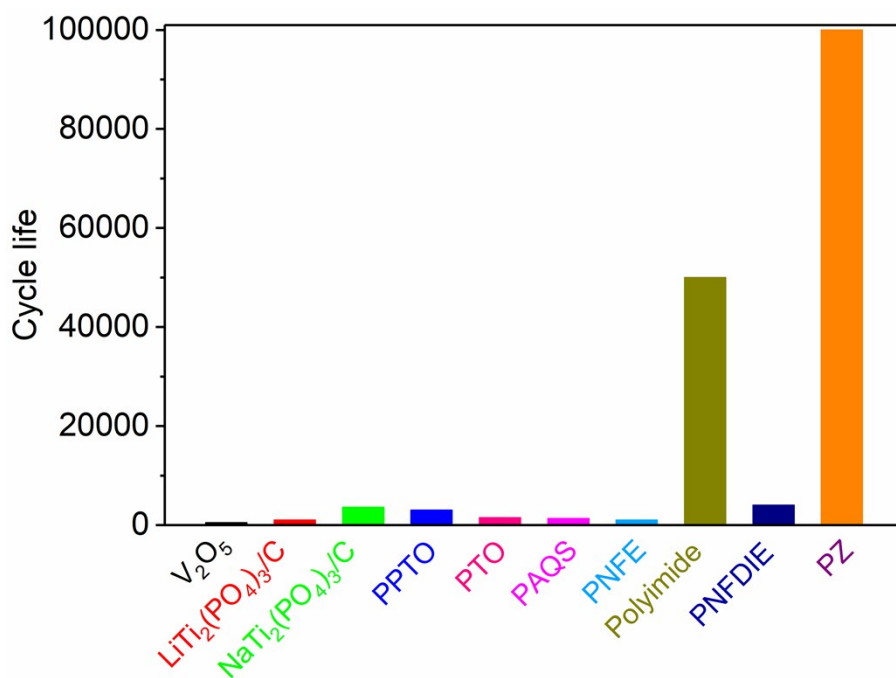


Fig. S3. Cycle life comparison of representative anode materials for ARBs.

The nPZ/KB anode demonstrated the ultra-high rate capability (102 mAh g⁻¹ at 100 C) and ultra-long cycle life (100,000 times for 100 C) compared with some representative anode materials in Fig. S3. Thus, the excellent electrochemical performance of the nPZ/KB demonstrated its practical values in large-scale energy storages.

Note 1.

Referred to some classic works,^{7, 11-13} the organic active mass in the electrode were ~60%. In order to compare with the results in the literatures, the active mass of phenazine in the nPZ/KB composite was chose to 70%. When preparing the nPZ/KB electrode, the 5% PTFE binder have to be added, so the active mass in the nPZ/KB anode was 66.5%.

In the article, all kinds of coin cell were fabricated as follows:

1) For the PZ/KB electrode, nPZ/KB electrode, nPZ/CB electrode, nPZ/CNT electrode, the mass weight of all the electrodes was 3~4 mg, and the active mass weight of phenazine in all the electrodes were ~ 2 mg. The area of all the electrodes was $1 \times 1 \text{ cm}^2$. The total thickness of the electrode and nickel foam current collector was ~ 135 μm , and the total thickness of the electrode and Ti mesh was ~ 231 μm .

2) NiOOH cathode and AC cathode was used respectively. For the NiOOH cathode, its area was $1 \times 1 \text{ cm}^2$, the thickness is ~ 667 μm and the mass is ~ 322 mg. For AC cathode, it was cut into the $\phi 16 \text{ mm}$ discs and pressed onto the nickel foam or Ti mesh, and the total thickness was ~699 and ~680 μm , respectively.

3) The batteries were assembled in CR2016 type coin cells using the absorptive glass mat (AGM) separator. The spongy AGM separator was cut into the $\phi 19 \text{ mm}$ discs and its initial thickness was ~ 1.2 mm. The electrolyte (~ 100 μL) was added to the battery

system. Furthermore, the thick spongy AGM separator was benefit to achieve the tight contact between electrode and battery cell shells.

4) Similarly, the nPDBM/KB-AC coin cell was assembled with the same method above.

5) The nickel foam current collector was used in the alkaline electrolytes and Ti mesh was used in the neutral electrolytes.

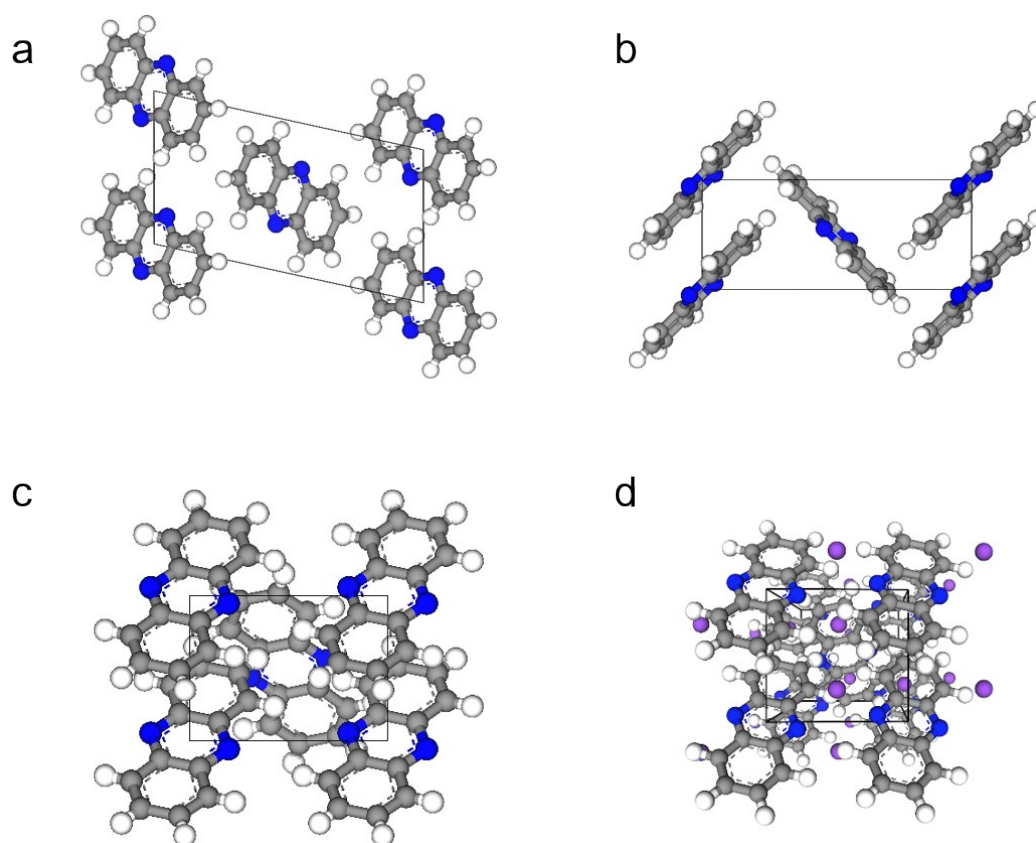


Fig. S4. Crystal structure of phenazine according to single crystallographic data from Cambridge Structural Database (CSD entry: PHENAZ04)¹⁴. Top view and side view of phenazine.

Density-functional theory simulation

The crystalline structures of phenazine-Na was calculated using density-functional theory (DFT) implemented in the CASTEP module of Materials Studio 7.0.¹⁴⁻¹⁶ The generalized gradient approximation (GGA) in the form of Perdew–Burke–Ernzerhof (PBE) was selected as the exchange-correlation functional.^{17, 18} Grimme dispersion correction was employed in all calculations to describe van der Waals (vdW) and π -

stacking interactions.^{19, 20} The lattice dimensions were optimized simultaneously with the geometry. A plane wave energy cutoff of 700 eV and the Monkhorst-Pack k -point grid of $2 \times 2 \times 1$ were used. The convergence criteria for energy, force, stress and displacement are 5×10^{-5} eV/atom, 0.03 eV/Å, 0.05 GPa and 1×10^{-3} Å, respectively. All simulation works were performed using the computing resources at National Supercomputing Center in Shenzhen.

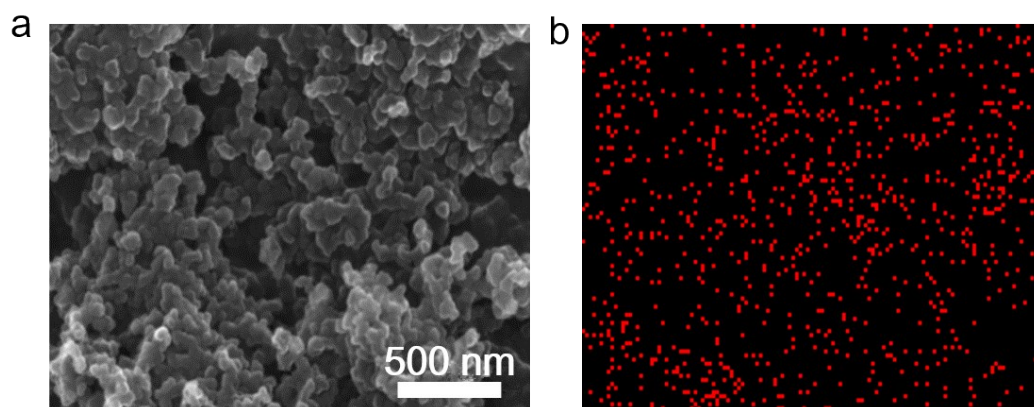


Fig. S5. Morphological features of nPZ/KB composite. (a) SEM and (b) corresponding EDX mappings of the elemental distribution of N in the nPZ/KB composite.

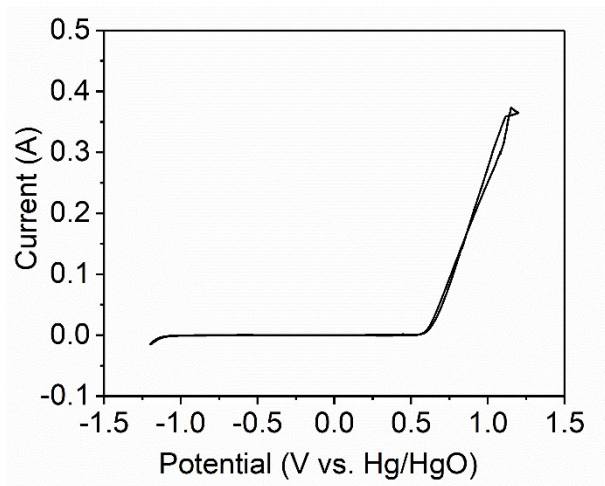


Fig. S6. CV curves of the Ni collector in the 6 M KOH electrolyte at 1mV s^{-1} .

As shown in Fig. S6, the electrochemical window of the 6 M KOH electrolyte was from $\sim -1.12\text{ V}$ to $\sim 0.56\text{ V vs. Hg/HgO}$. So the H_2 evolution and O_2 evolution side reactions could be successfully avoided within the voltage ranges for the CV test.

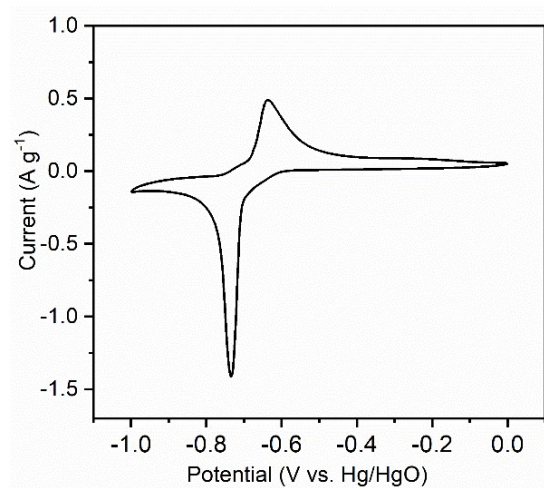


Fig. S7. Cyclic voltammograms of nPZ/CB composite electrodes at a scan rate of 0.5 mV s⁻¹ in 6 M KOH solution.

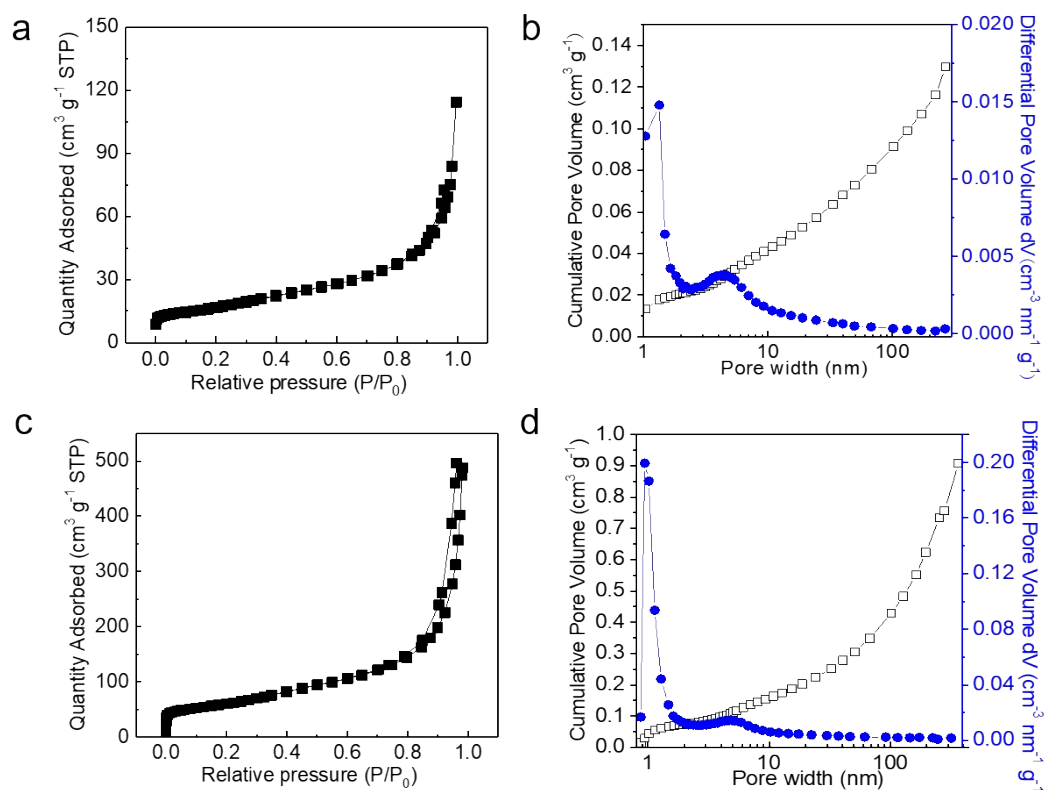


Fig. S8. The N₂ adsorption/desorption isotherms, cumulative pore volume and pore size distribution curves (calculated by using a DFT model) of (a, b) CB and (c, d) CNT.

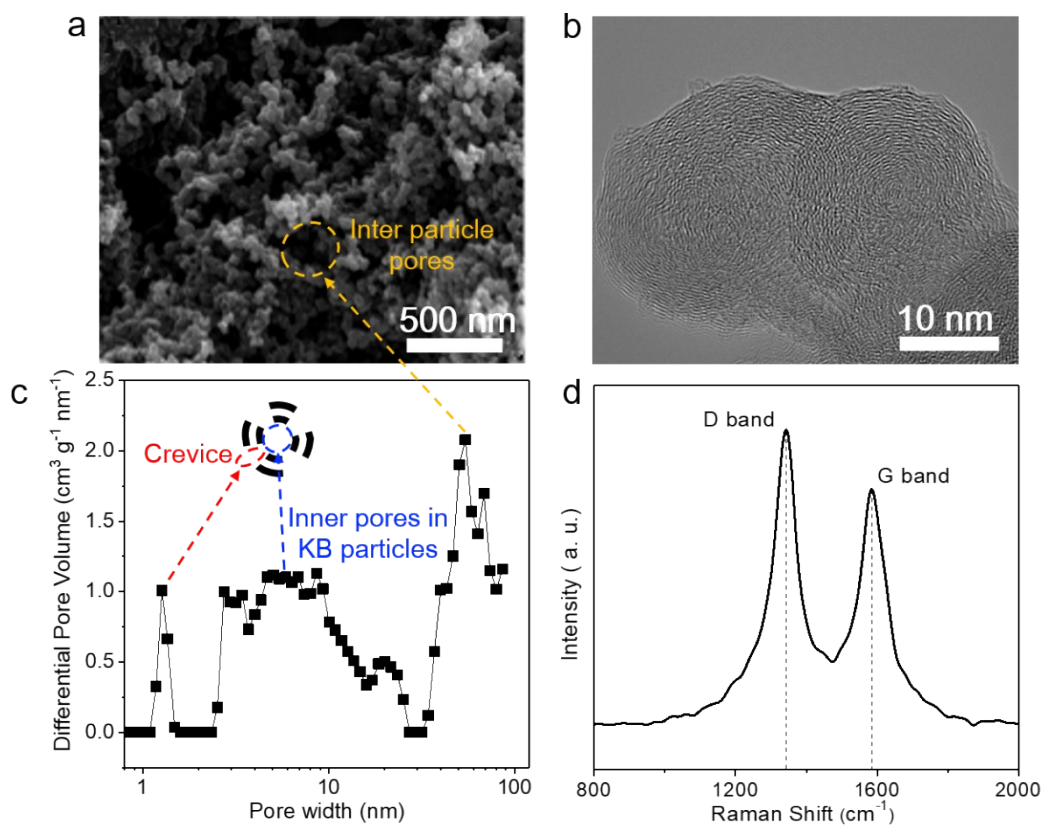


Fig. S9. Comprehensive characterizations of KB. (a) SEM image, (b) TEM image, (c) pore size distribution calculated by the N_2 -adsorption characterization, (d) Raman spectrum. The inset of (c) depicts the microstructure of one KB particle, indicating the contribution of various pores.

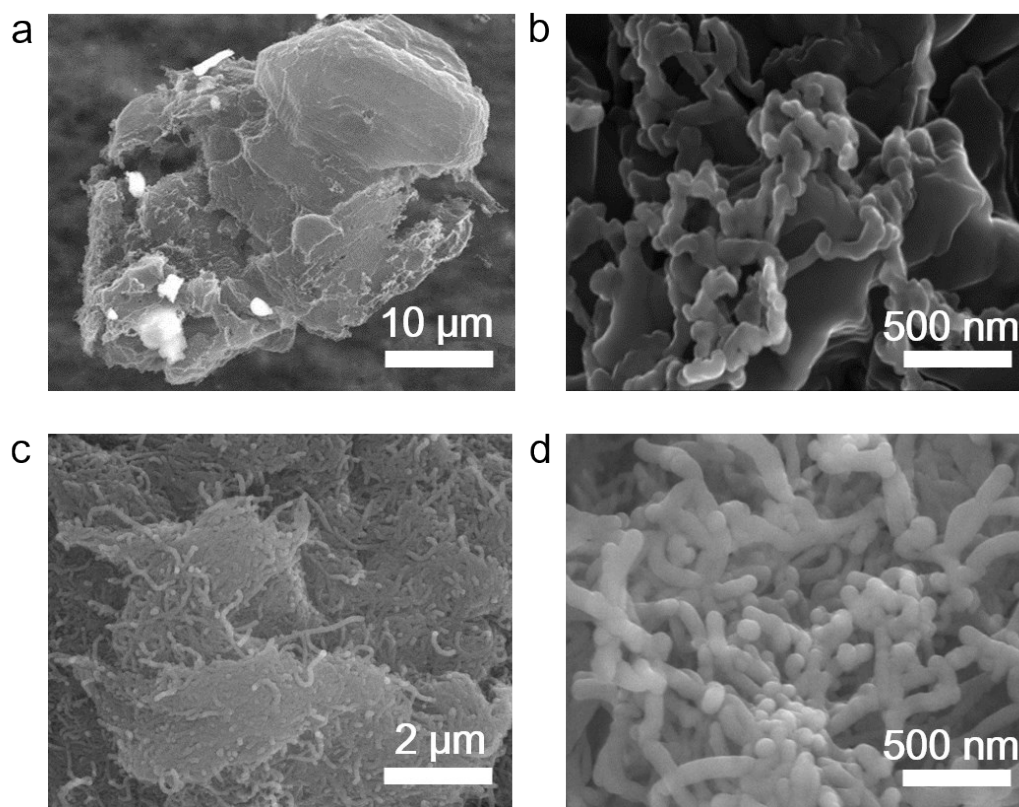


Fig. S10. SEM images of (a) commercial phenazine, (b) nano phenazine, (c) and (d) nPZ/CNT. Nano phenazine and nPZ/CNT were prepared by the same procedure with nPZ/KB, while the former was precipitated with no carbon additives and the latter was prepared by simply substituting KB with carbon nanotube (Cnano Technology Corp.).

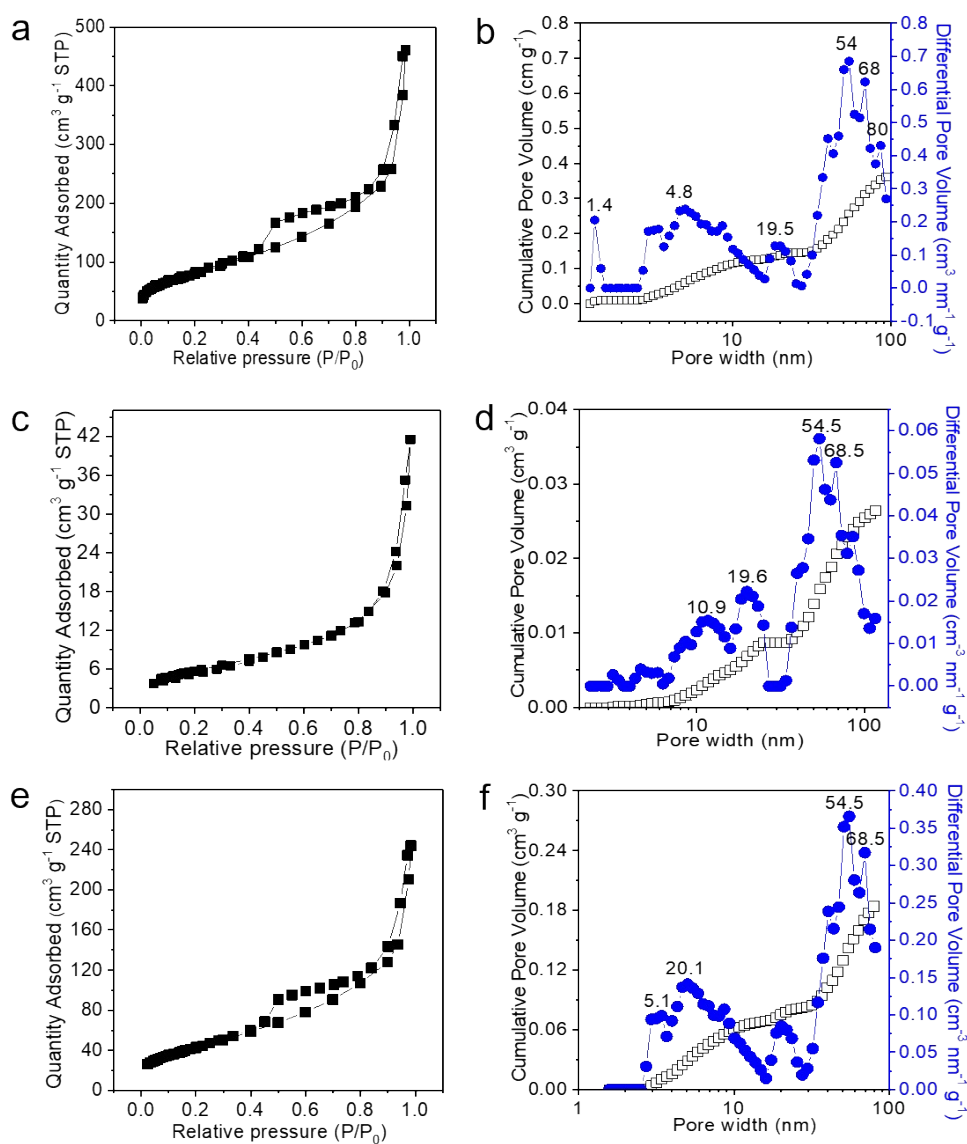


Fig. S11. The N₂ adsorption/desorption isotherms, cumulative pore volume and pore size distribution curves (calculated by using a DFT model) of (a), (b) nPZ/KB, (c), (d) nPZ/CB and (e), (f) nPZ/CNT.

Table S2 Characteristic surface areas and pore structures of the KB, nPZ/KB, nPZ/CB, and nPZ/CNT composites.

Sample	BET surface area (m ² g ⁻¹)	Total pore volume (cm ³ g ⁻¹) ^[a]	External pore volume (cm ³ g ⁻¹) ^[b]	Average pore width (nm)
KB	1386	2.54	1.49	10.0
CB	60.19	0.177	--	11.8
CNT	214.88	0.908	--	16.9
nPZ/KB	277.6	0.71	0.67	10.3
nPZ/CB	20.63	0.064	0.053	12.5
nPZ/CNT	148.4	0.38	0.37	10.2

^[a] Total pore volume measured at $P/P_0 = 0.99$. ^[b] External pore volume: volume of pores larger than 50 nm, determined by DFT model.

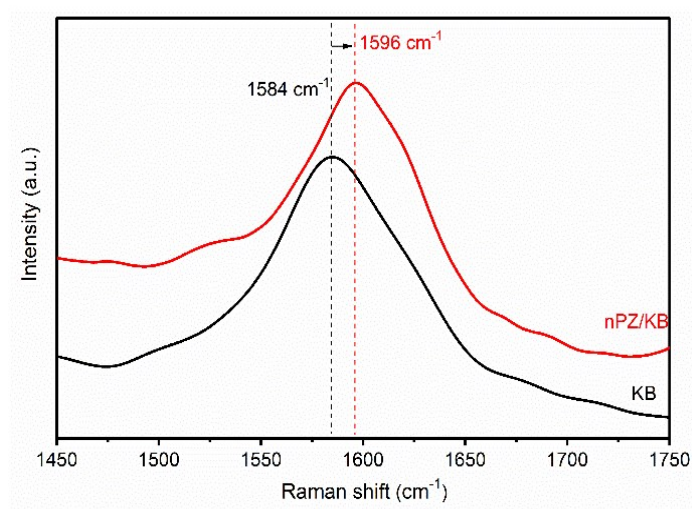


Fig. S12. Raman spectra of KB and nPZ/KB at the laser excitation of 532 nm.

Additionally, we observed π - π interactions between aromatic PZ molecules and KB using Raman spectroscopy. The G-band of KB after dissolution-precipitation process was up-shifted by 12 cm⁻¹ compared to that of pristine KB (Fig. S12). The up-shifts of the Raman spectrum for KB may stem from the changes in the number of π -electrons of KB,²¹ which strongly indicates π - π interactions between KB and aromatic PZ molecules. Consequently, it successfully raised electronic conductivity of PZ (as shown in Table S4) and inhibited the dissolution of PZ into aqueous electrolyte to some extent.

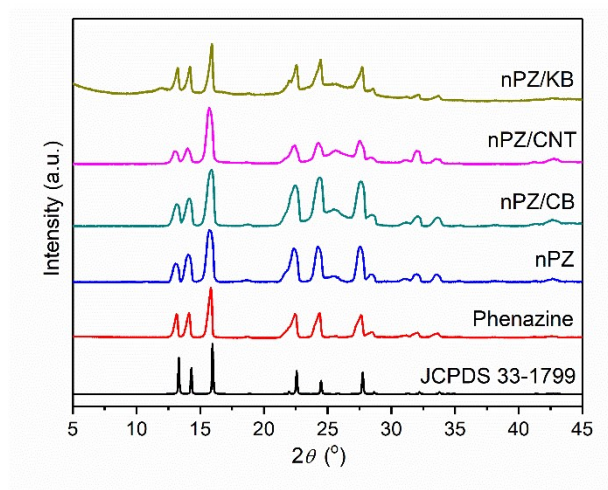


Fig. S13. XRD patterns of phenazine, nPZ, nPZ/CB, nPZ/CNT and nPZ/KB.

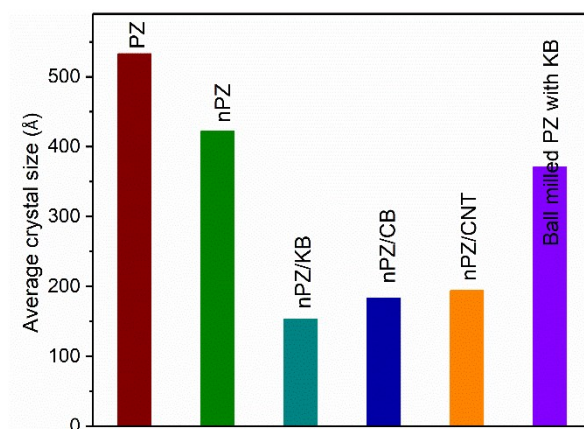


Fig. S14. The average crystal size of phenazine, nPZ, nPZ/KB, nPZ/CB, nPZ/CNT, and ball milled PZ and KB, calculated by Scherrer formula according to the XRD results in Fig. S13.

Table S3. The average crystal size of different phenazines and phenazines in various PZ/carbon composites

Sample	PZ	nPZ	nPZ/KB	nPZ/CB	nPZ/CNT	Ball milled PZ and KB
Average crystal size (Å)	533	422	153	183	194	371

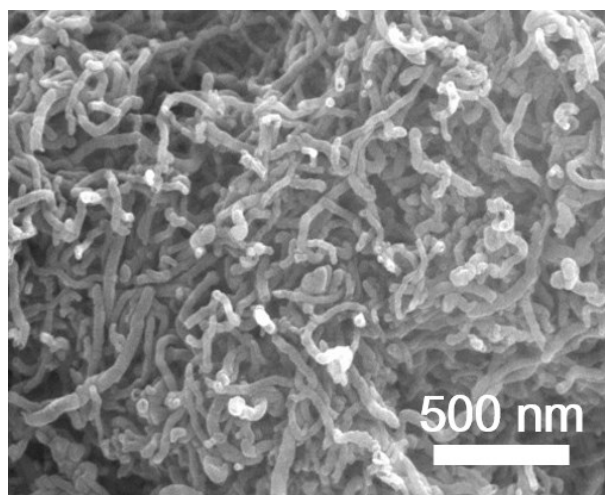


Fig. S15. SEM of the CNTs.

Table S4. Electronic conductivity of different carbon materials and PZ/carbon composites

Samples	Electronic conductivity (S cm ⁻¹)		
	1MPa	2MPa	3MPa
KB	241	324	458
CB	195	217	245
CNT	381	413	519
PZ	2.71×10^{-6}	2.92×10^{-6}	3.50×10^{-6}
nPZ/KB	65.0	73.0	87.0
nPZ/CB	34.2	55.1	71.9
nPZ/CNT	17.9	23.3	28.4
Ball milled PZ and KB	1.62	1.82	2.07

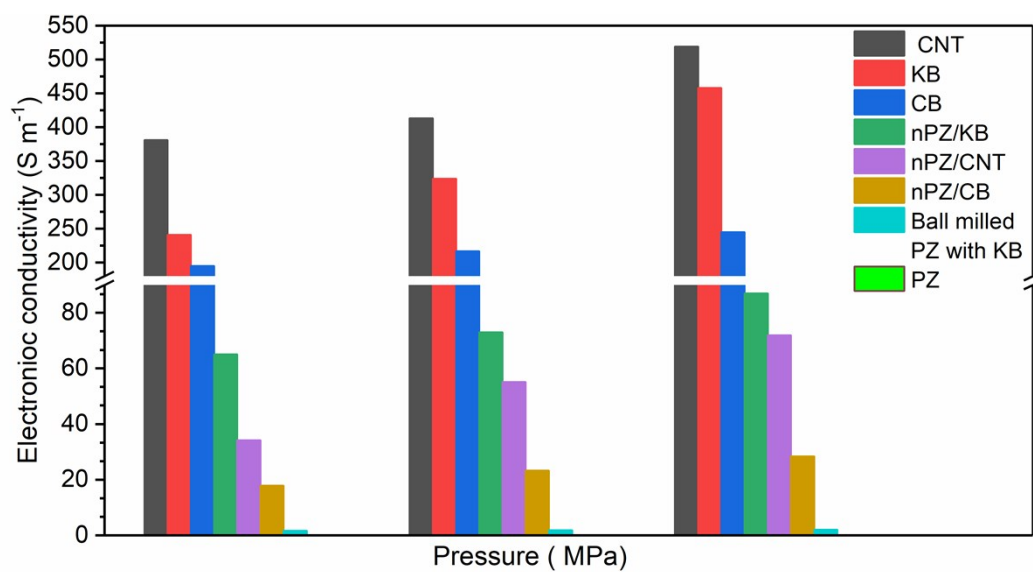


Fig. S16. The electronic conductivity of different carbon materials and PZ/carbon composites.

Note 2.

Most organic active materials exist the shortcoming of low electronic conductivity (2.71×10^{-6} S cm⁻¹ for PZ), which will seriously restrict the specific capacity and rate capability. Fabricating organic/conductive carbon composites is an effective way to tackle this issue. KB, CB and CNT are common conductive binders, and their electronic conductivity (458, 245, and 519 S cm⁻¹ respectively) are shown in Table S4 and Figure S16. Through the in-situ dissolution-precipitation process, nPZ/KB, nPZ/CB and nPZ/CNT composites were successfully prepared with significantly boosted electronic conductivity 458, 245, and 519 S cm⁻¹ at 3 MPa, respectively.

CNT showed a hollow tubular structure with an intertwined morphology (Fig. S15) and delivered the highest electronic conductivity (Table S4). However, phenazine on CNT surface is easy to form the large agglomerations, which hindered the effective connections of CNT in the bulk phase of nPZ/CNT composite (Fig. S10c, d and Fig. 3). Thus, the electron transferring of CNT was severely impeded. Meanwhile, CB delivered the smallest specific surface area (60.19 m² g⁻¹) and total pore volume (0.177 cm³ g⁻¹) among KB, CB and CNT in Table S2. It would not be beneficial for the in situ precipitation of PZ, so nPZ/CB delivered the larger average crystal size (183 Å) shown in Table S3. What's worse, the lowest electronic conductivity of CB (245 S cm⁻¹) was also not be helpful to obtain the high electrochemical performance of nPZ/CB anode. Comparatively, KB possessed a clusters morphology with the particle size of ~ 20 nm

(Fig. S9a and b), and presented high BET surface area ($1386 \text{ m}^2 \text{ g}^{-1}$) and pore volume ($0.00254 \text{ cm}^3 \text{ g}^{-1}$, Table S2), which was beneficial for the uniform precipitation of nano-phenazine on KB surface. In addition, the nPZ/KB possessed the smallest average crystal size (153 \AA) shown in Table S3. This results demonstrated that by the novel in-situ dissolution-precipitation method, PZ was not only uniformly precipitated on the surface of KB, but also cannot influence the free connection between KB monomers and the formation of effective electron-transferring pathways. (Fig. S5 and Fig. 3). Hence, the nPZ/KB composite delivered the higher electronic conductivity and exhibited more excellent electrochemical performances than nPZ/CB and nPZ/CNT. Naturally, KB was ought to be the best conductive material among KB, CB and CNT.

Note 3.

As shown in Fig. 3a, during redox reactions, two N atoms in phenazine would reversibly accepted/released two electrons accompanied by the coordination with two metal ions and previous researches.¹² So its theory specific capacity was calculated as follows equation:

$$C_t = \frac{5}{18} \times \frac{2F}{M} \quad (1)$$

Where C_t represented the theory specific capacity of phenazine, mAh g⁻¹, F represented Faraday constant, 96,485 C mol⁻¹, M represented the molar weight of phenazine, 180.21 g mol⁻¹. Hence, the theory specific capacity of phenazine was 298 mAh g⁻¹ according to the equation (1).

Hence, 1 C current density was defined as 298 mA g⁻¹ based on the weight of phenazine in the anode.

In this article, we mainly focused on the electrochemical properties of phenazine anode. So, all the specific capacities reported in the manuscript and Supporting Information were calculated based on the mass weight of phenazine in the anode.

The capacity of corresponding cathode was much larger than that of the anode in full battery. The weight of active phenazine in anode was ~ 2 mg while the weight of NiOOH and AC cathode was ~322 mg and ~ 73 mg, respectively. Therefore, the

specific energy density of full battery was calculated based on the weight of phenazine in the nPZ/KB anode according to the Equation 2¹².

$$E_{spe} = \frac{C \times V \times 1000}{m} \quad (2)$$

where E_{spe} is the specific energy density (Wh kg⁻¹); C is the discharge capacity (mAh); V is the average discharge voltage (V); m is the active mass (mg) of phenazine in the nPZ/KB anode.

For the nPZ/KB-NiOOH battery, the active mass of NiOOH cathode and nPZ/KB anode was 322 mg and 2 mg, respectively. The average discharge voltage was 1.06 V. So the specific energy density of the nPZ/KB-NiOOH battery was 303.16 Wh Kg⁻¹.

For the nPZ/KB-AC battery, the active mass of AC cathode and nPZ/KB anode was 73.1 mg and 2 mg, respectively. The average discharge voltage was 0.48 V. So the specific energy density of the nPZ/KB-AC battery was up to 154.56 Wh Kg⁻¹.

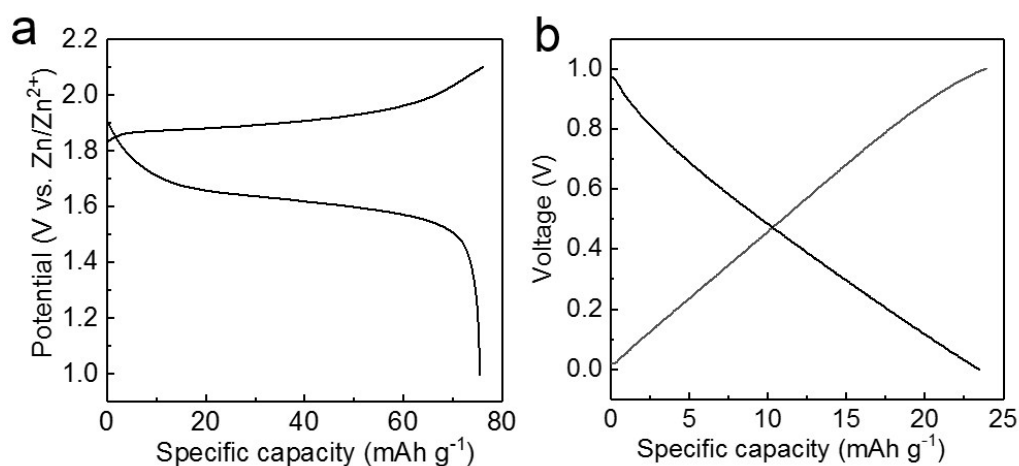


Fig. S17. The voltage profiles of NiOOH cathode and AC cathode. (a) The voltage profiles of AC-AC battery at the current of 1 mA in 6 M KOH; (b) The voltage profiles of NiOOH cathode at the current of 5 mA in 6 M KOH coupled with Zn cathode.

Similar to the half-cell test in organic systems like Li/Na/K ion batteries using excessive metal anodes, we also tried to test the specific capacity of nPZ/KB anode using the excessive cathode materials as the counter electrode. So, the nPZ/KB anode showed high specific capacity, even exceeding its theoretical capacity.

The specific capacity of the NiOOH and AC cathode was 75.5 and 23.5 mAh g⁻¹, respectively (Fig. S17). The weights of NiOOH and AC cathode in the nPZ/KB-NiOOH and nPZ/KB-AC systems were ~322 and ~73 mg, respectively. So the capacity of the NiOOH cathode was 24.3 mAh in the nPZ/KB-NiOOH and the capacity of the AC was 1.7 mAh in the nPZ/KB-AC system. In contrast, the corresponding capacity of the nPZ/KB anode (~2 mg) is about 0.6 mAh in this work. Though the area capacity of AC cathodes is not very high, its reaction mechanism is based on the capacitance behavior

of ion adsorption with the minimized electrode polarization. Thus, it is clear that the capacity of NiOOH or AC cathode greatly exceeded that of the nPZ/KB anode. So, the nPZ/KB-NiOOH and nPZ/KB-AC cell are both similar to a half cell (vs. Li/Li⁺ or Zn/Zn²⁺ electrodes). It is reasonable to characterize the capacity of nPZ/KB in these cells.

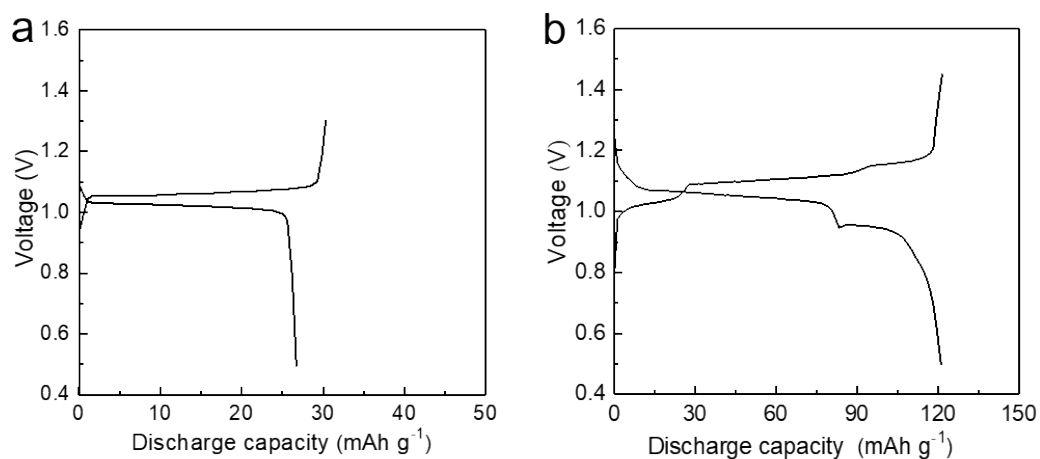


Fig. S18. Galvanostatic discharge/charge profiles of (a) nPZ/CB and (b) nPZ/CNT composite electrodes at the current rate of 0.2 C, respectively, during their tenth charge /discharge process in 6 M KOH.

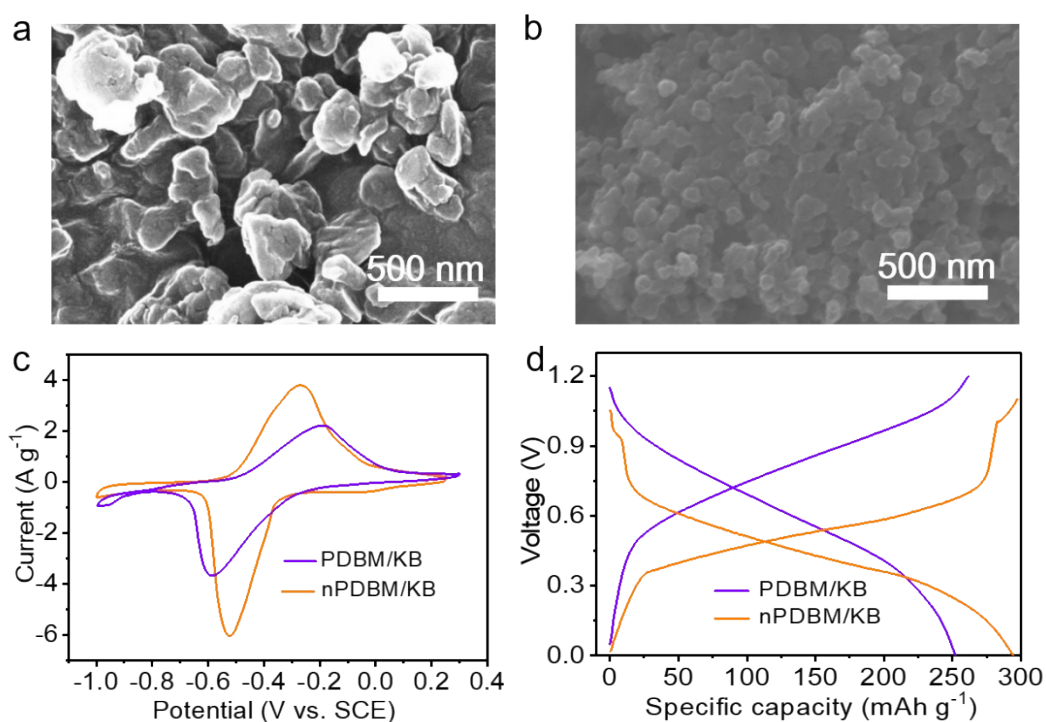


Fig. S19. Morphological and electrochemical properties of nPDBM/KB anode. (a) SEM of PDBM; (b) SEM of nPDBM/KB; (c) CV curves of PDBM/KB and nPDBM/KB in 1 M Li_2SO_4 //2 M ZnSO_4 electrolyte at 1 mV s^{-1} ; (d) Voltage profiles of PDBM/KB and nPDBM/KB at 1 C in 1 M Li_2SO_4 //2 M ZnSO_4 electrolyte coupled with AC cathode.

The novel in-situ dissolution-precipitation method was suit for a diversity of organic redox-active materials by another works below, which indicates that the in-situ dissolution-precipitation method would be a promising technique for the preparation of organic compounds/KB electrode composites for aqueous rechargeable batteries.

In order to demonstrate the universality of the in-situ dissolution-precipitation method, the nano poly (2,5-dihydroxy-1,4-benzoquinone-3,6-methylene)

(nPDBM)/KB composite was also prepared by the in-situ dissolution-precipitation method. Firstly, PDBM was synthesized through the condensation polymerization of 2,5-dihydroxy-1,4-benzoquinone and methanol. Secondly, 0.6 g PDBM was dissolved into 20 mL N,N-Dimethylformamide (DMF) solvent by magnetic stirring. Thirdly, 0.4 g KB was added into the solution under rapid stirring for 10 min. Subsequently, the mixture was treated under ultrasonic for 30 min so that KB could be dispersed uniformly in the solution. Then, 450 mL DI water was added slowly at the rate of $10 \mu\text{L min}^{-1}$ under rapid stirring. Finally, the as-prepared nano-PDBM/KB (nPDBM/KB) was filtered, washed with excess DI water and then dried under freeze-drying for 24 h.

As shown in Figure S19a, the as-prepared PDBM showed a particle size of 300 ~ 400 nm. Using the in-situ dissolution-precipitation method, the nano-PDBM can be uniformly precipitated on the KB surface and the nPDBM/KB composite showed a small particle size of ~ 60 nm (in Fig. S19b). Meanwhile, the nPDBM/KB anode delivered the higher reaction kinetics and smaller electrochemical polarization (Fig. S19c), which was similar to that of nPZ/KB anode. What's more, nPDBM/KB delivered a higher specific capacity of 294 mAh g⁻¹ than that of PDBM/KB (255 mAh g⁻¹), shown in Fig. S19d.

So, the in-situ dissolution-precipitation method is a universal and powerful technique to prepare the organic compound/porous carbon composite. Benefited from

this novel method, the particle size of the organic compounds not only can be reduced to ~ 80 nm, but also the organic compounds can precipitate on carbon conducting host surface uniformly, ensuring excellent electrochemical properties.

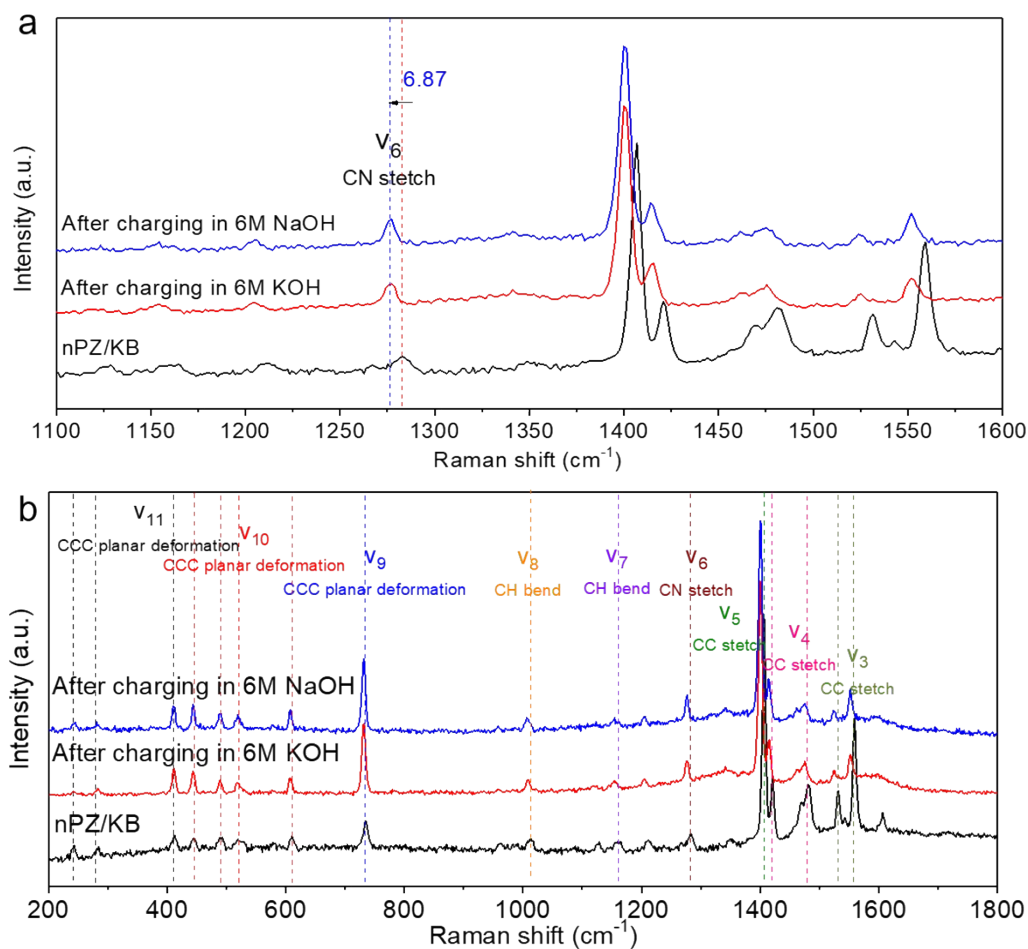


Fig. S20. Raman spectra of the nPZ/KB anode before and after charging in 6 M KOH and 6 M NaOH with the wavenumbers (a) from 1100 to 1600 cm^{-1} and (b) from 200 to 1800 cm^{-1} .

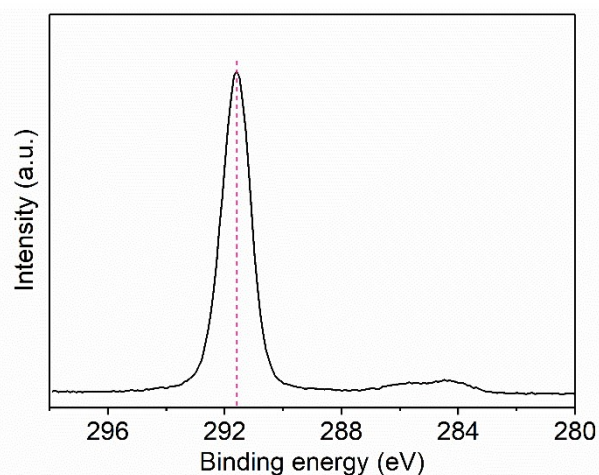


Fig. S21. The C1s XPS spectra of PTFE.

In order to exclude the C1s spectra of CFx in the PTFE binder, the XPS spectra of PTFE was characterized separately. As shown in Fig. S21, there is indeed the C1s peak of CFx at 291.6 eV. However, the content of PTFE binder in the electrode was only 5%, so the peak intensity of the CFs was very weak compared with the other peaks of the electrode. Thus, the pristine electrode do not show a visible peak at around 292 eV.

It could be clearly seen in Fig. 4c that the peak intensity of K2p increased obviously after 100% SOC and then decreased close to the initial state after the 100% DOD, verified the reversible coordination/un-coordination reactions of K^+ with phenazine.

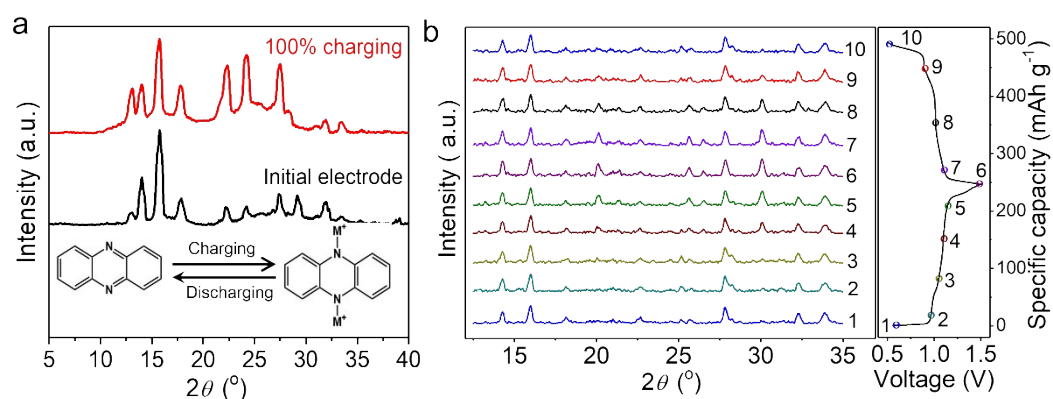


Fig. S22. (a) XRD patterns of nPZ/KB electrode before and after charging. (b) In-situ XRD patterns and the corresponding voltage profile during the charging-discharging process.

XRD patterns of the prepared nPZ/KB electrodes before and after 100% charging were shown in Fig. S22a, the peaks at 22.3° , 24.2° , and 27.5° were strengthened tremendously. Furthermore, in-situ XRD was carried out to trace the phase evolution in a series of charging-discharging state (Fig. S21b). Peaks at 20.1° , 25.1° , 26.5° , and 30.0° reversibly appeared-disappeared, indicating the reversible phase evolution of nPZ/KB.

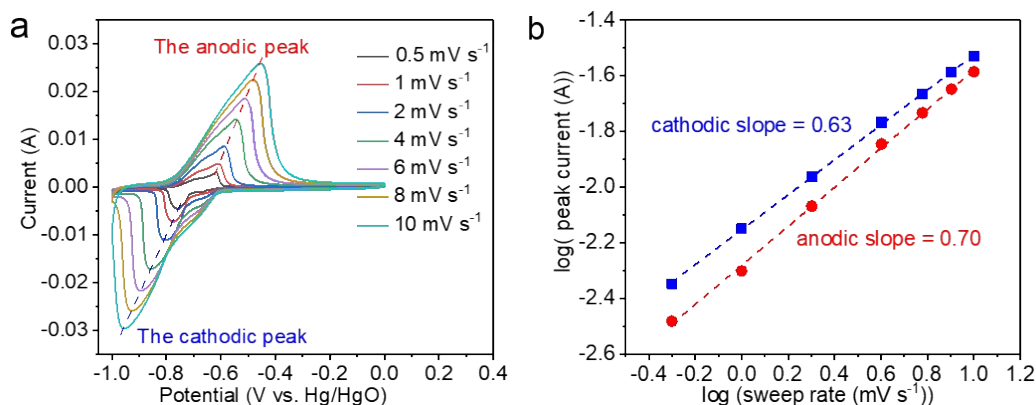


Fig. S23. The cyclic voltammetry analysis of the nPZ/KB anode at various scan rate. (a) CV curves of the nPZ/KB anode at different scan rates in 6 M KOH electrolyte; (b) Logarithmic relationship of the peak current with the scan rate for the anodic and cathodic peaks labeled in Figure S23a.

The peak current (i) and the corresponding sweep rate (ν) will meet the following equation 3:

$$i = a\nu^b \quad (3)$$

where a and b are both constants. The b value is an indicator of diffusion control (close to 0.5) or capacitive effect (close to 1) and it is determined by the slope of the $\log(\nu)$ - $\log(i)$.

According to Eq. (3), the corresponding b values of the nPZ/KB were calculated to be 0.70 and 0.63 in 6 M KOH electrolyte, indicating that there are diffusion-controlled and surface-controlled progress simultaneously, and the diffusion controlled progress dominates the electrochemical reaction.

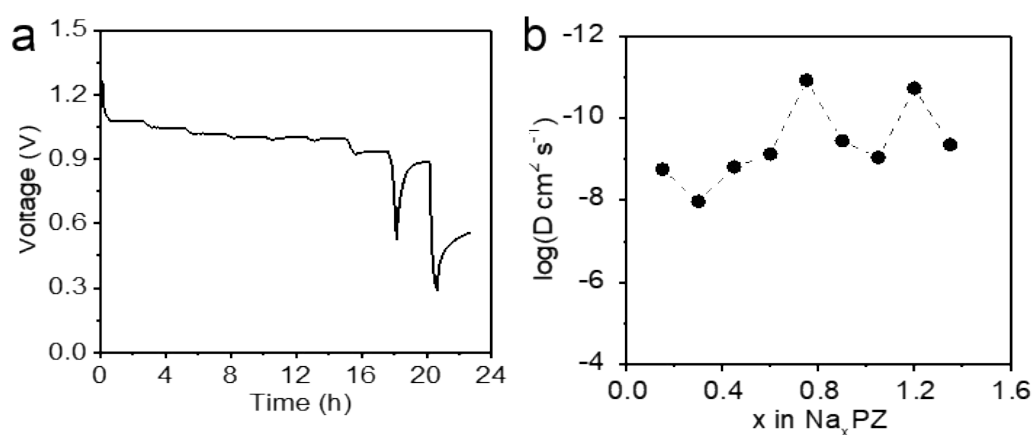


Fig. S24. Diffusion coefficients of Na⁺ measured with GITT. (a) The GITT potential profile for nPZ/KB in the 6 M NaOH electrolyte (in terms of charge state in the 2nd cycle). (b) Diffusion coefficients calculated from the GITT potential profiles for phenazine in the nPZ/KB composite in 6 M NaOH.

To further explore the reasons for high rate capacity and excellent prolonged cycle life of nPZ/KB anode, we have employed the galvanostatic intermittent titration technique (GITT) to measure the apparent diffusion coefficient of Na⁺ ions in nPZ/KB anode with a pulse current density of 0.1~0.17 C for 0.5 h. The rest interval was 2 h between the charging and discharging process. The diffusivity coefficient of Na⁺ ions (D_{Na^+}) can be estimated based on Fick's second law with the following simplified equation:

$$D = \frac{4}{\pi\tau} \left(\frac{m_B V_M}{M_B S} \right)^2 \left(\frac{\Delta E_s}{\Delta E_\tau} \right)^2 \quad (4)$$

where τ is the pulse duration, m_B and M_B are the active mass and molar mass of phenazine, V_M is the molar volume, and S is the active surface area of the nPZ/KB anodes. ΔE_S and ΔE_τ are the change of quasi-equilibrium voltage and battery voltage, which can be obtained from the GITT curves as shown in Fig. S24a.

As shown in Fig. S24b, the calculated $D_{(\text{Na}^+)}$ was ranging from $2.8 \times 10^{-10} \text{ cm}^2 \text{ s}^{-1}$ to 4.92×10^{-8} , which was almost one order of magnitude higher than the value reported in the literature⁹. The high ion diffusion coefficient of Na^+ in phenazine was attributed to the uniform precipitation of nano-phenazine on the KB surface. It further demonstrated the superiority of our dissolution-precipitation method.

Table S5. E_{HUMO} and E_{LUMO} of PZ, PZ-K and PZ-Na.

	PZ	PZ-K	PZ-Na
E_{HUMO}	-6.32 eV	-6.48 eV	-6.52 eV
E_{LUMO}	-2.76 eV	-2.98 eV	-3.04 eV

Note 4

As reported previously, the redox potentials of PZ is proportional to proportional to the LUMO energy (E_{LUMO}) and E_{HUMO} energy of the molecule.²² According to the results in Table S5, the E_{LUMO} of PZ was -2.76 eV, which was a little higher than that of half-reduced PZ-K, indicated the existing sequent two-step reduce reaction. Comparatively, the calculated E_{HUMO} of PZ (-6.32 eV) and PZ-K (-6.48 eV) also demonstrated the two-step oxide reaction during the charge-discharge process. Similar results also achieved when the electrolyte was transferred to 6 M NaOH. Thus, it was reasonable that there existed two plateaus during the charging-discharging process.

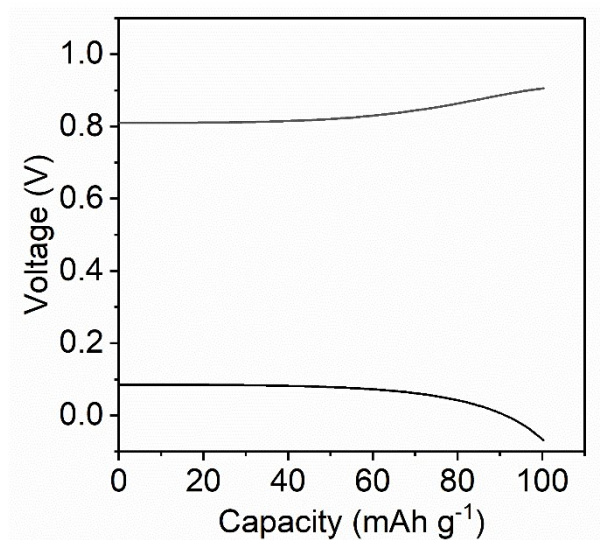


Fig. S25. Voltage curves of the nPZ/KB-AC full battery at 100 C.

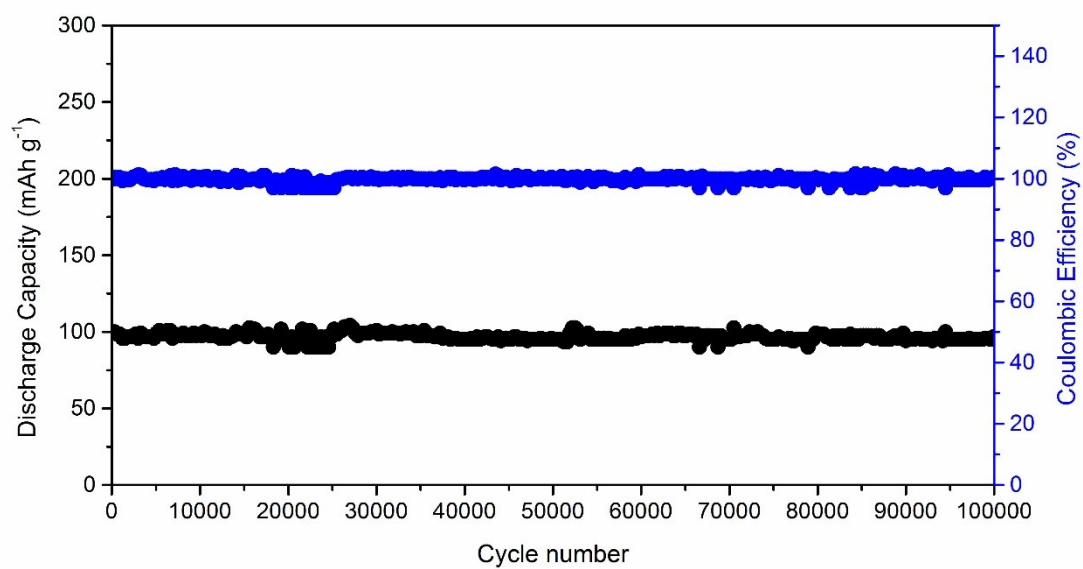


Fig. S26. Cycle properties of the nPZ/KB anode in 6 M KOH at 100 C.

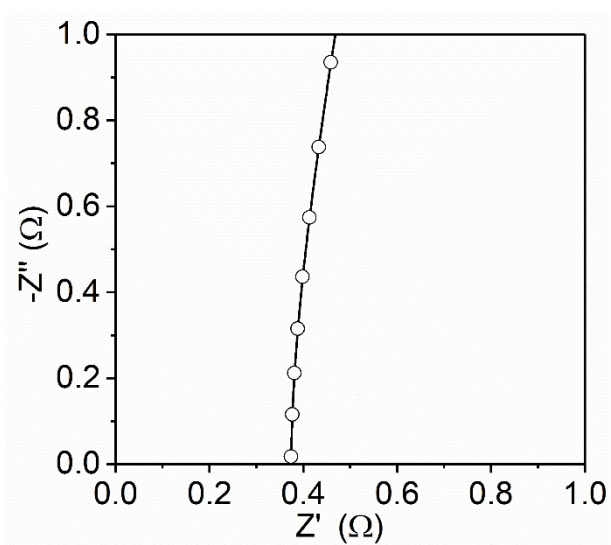


Fig. S27. Nyquist plots for the blank battery with 6 M KOH electrolyte and AGM separator in the 2016 coin cell.

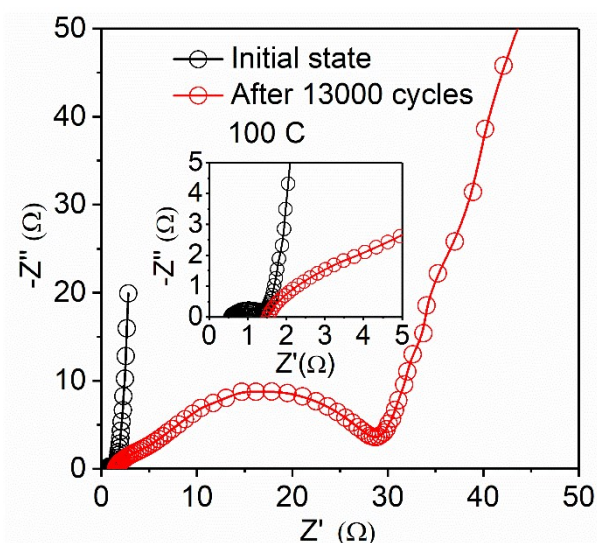


Fig. S28. Nyquist plots the nPZ/KB-AC coin battery before and after cycling 13,000 times at 100 C.

The nPZ/KB electrode with the area of 1 cm^2 was 3~4 mg, while the active mass content was 66.5%. So the active mass in the nPZ/KB electrode was $\sim 2 \text{ mg}$, and the areal capacity of the nPZ/KB electrode was $\sim 0.6 \text{ mAh cm}^{-2}$. At the current rate 100 C, the current was 60 mA for the working electrode of 1 cm^2 area. Furthermore, as shown in Fig. S27, the total ohmic resistance (the sum of the resistance of the blank CR2016 coin cell with 6 M KOH electrolyte and AGM separator) was only 0.37Ω . As shown in Fig. S28, the total ohmic resistance of the nPZ/KB-AC coin cell was 0.55Ω . Consequently, the ohmic polarization would be only 33 mV.

Hence, at the high-rate of 100 C, the charge transferring resistance of battery would be the main resistance in the total resistance. Even after 13,000 cycles, the ohmic resistance still kept the low value of 1.55Ω (Fig. S28). Therefore, the ohmic resistance

would not significantly decrease the specific capacity of the nPZ/KB-AC coin even at the high-rate of 100 C (Fig. S25 and Fig. S28).

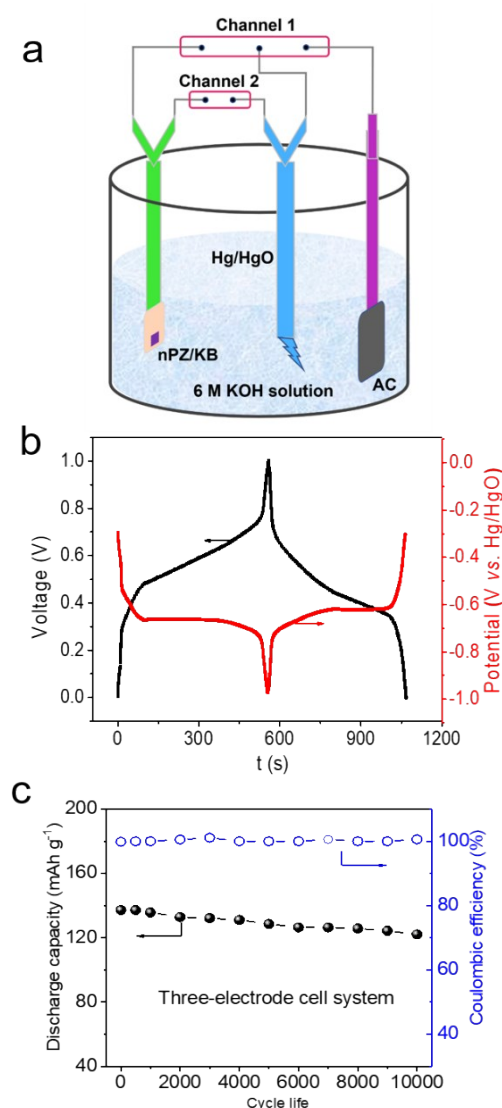


Fig. S29. The electrochemical properties of the nPZ/KB anode in 6 M KOH solution. (a) The scheme and (b) the charging-discharging curves of nPZ/KB-AC battery and corresponding potential changes (vs. Hg/HgO) at 100 C (the charging-discharging process of the AC-nPZ/KB battery in the voltage range of 0 ~ 1.0 V was controlled by the channel 1, the changes of the potential (vs. Hg/HgO) for the nPZ/KB anode was detected by the channel 2); (c) The cycling stability of nPZ/KB in the voltage range of -0.9 ~ -0.3 V at 100 C with three-electrode cell system.

Fig. S29a illustrated the apparatus for modelling the charging/discharging process and detecting the absolute potential of PZ simultaneously. The charging/discharging process was tested with electrochemical measurement channel 1, which simulates the charging/discharging states of nPZ/KB in ordinary coin cell. In order to detect the practical working voltage, the potential between nPZ/KB anode and Hg/HgO electrode was measured with channel 2. With the nPZ/KB-AC system charge/discharge in the voltage range of 0.0 - 1.0 V at 100 C, the corresponding nPZ/KB available potential range (vs. Hg/HgO) is -0.9 ~ -0.3 V (Fig. S29b). Then, the long cycling performance of nPZ/KB anode was measured in the potential range of -0.9 ~ -0.3 V (vs. Hg/HgO) at 100 C by a three-electrode cell system. The result showed that nPZ/KB electrode demonstrated good cycling performance with the capacity retention of 89.0% in the three-electrode system, and the coulombic efficiency is nearly 100% in the whole time (Fig. S29c).

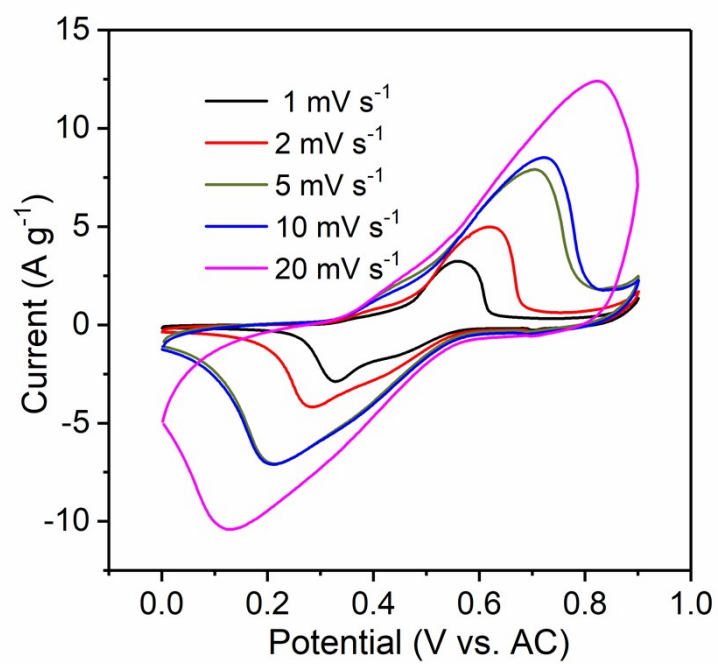


Fig. S30. CV curves of the nPZ/KB-AC full battery at different scan rates in 6 M KOH.

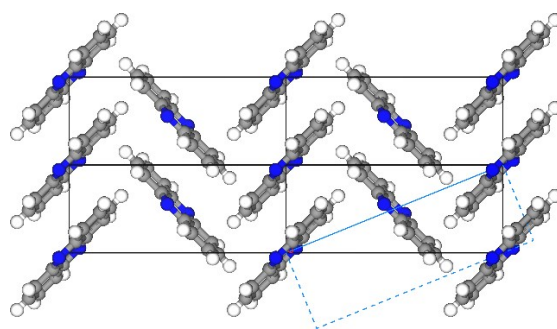


Fig. S31. Crystal structure of phenazine after 10000 cycles.

The increased intensity of (011) lattice plane for phenazine after 10,000 cycles is due to the improved accumulation intensity and crystallinity of phenazine, which means that the repeated charging/discharging process is benefit to the rearrangement of phenazine molecule and the decrease of molecule spacing, and further improving the accumulation intensity and crystallinity.

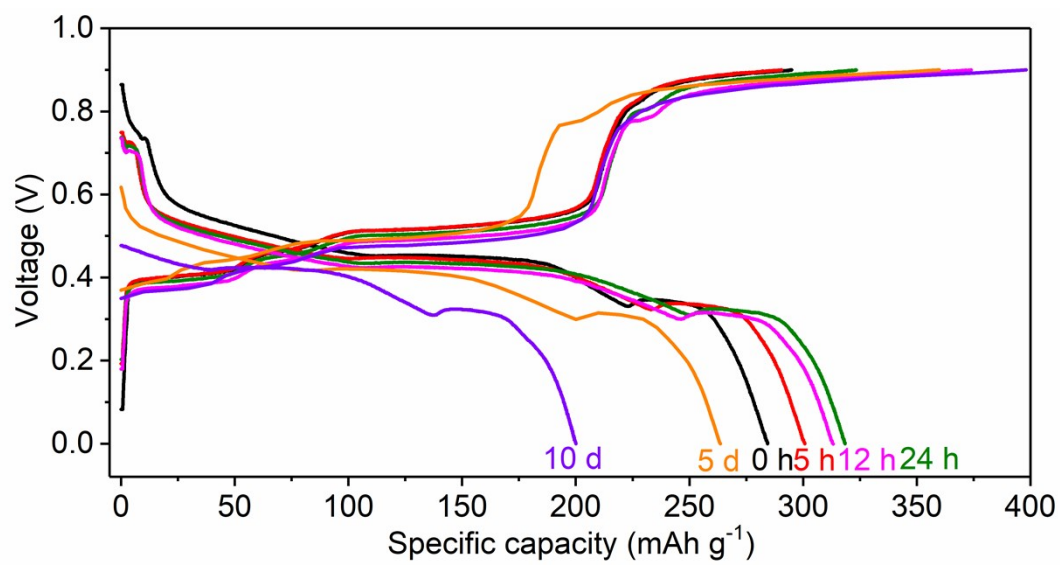


Fig. S32. Investigation of the nPZ/KB anode self-discharge properties.

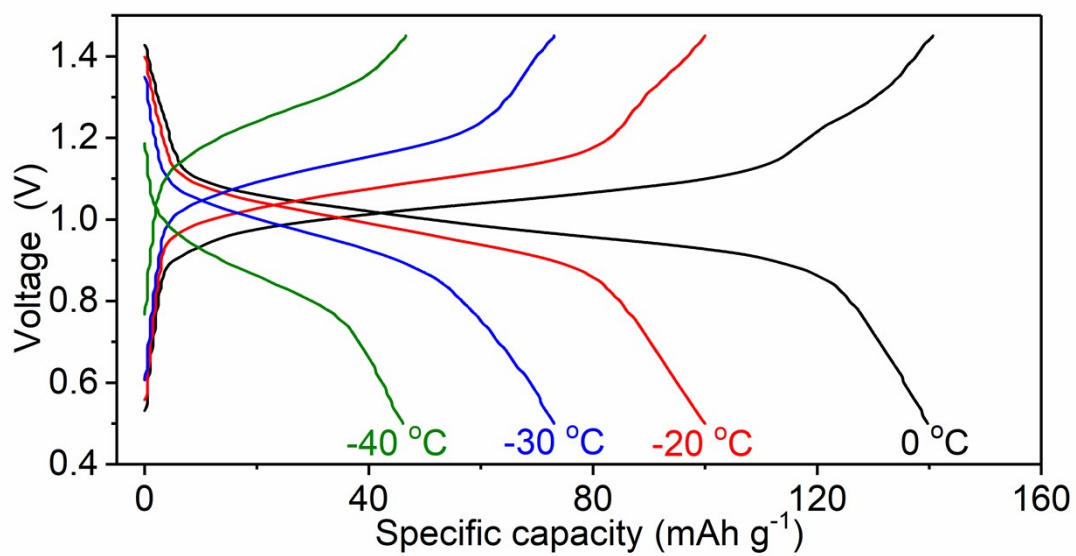


Fig. S33. Voltage profiles curves of nPZ/KB-NiOOH cell at low temperatures.

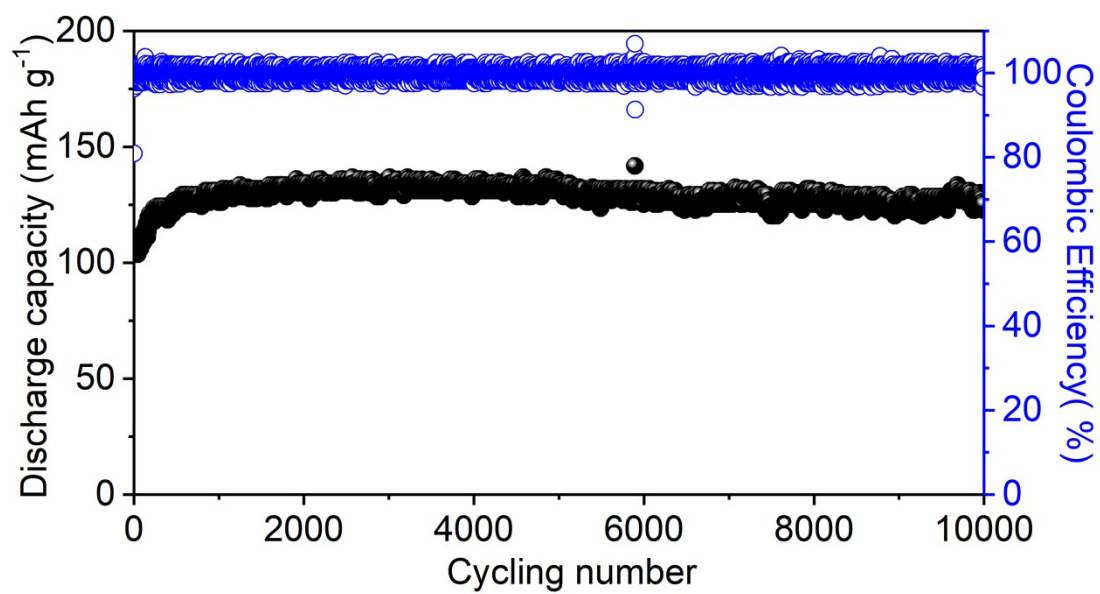


Fig. S34. Cycle properties of nPZ/KB anode in 6 M NaOH at 10 C.

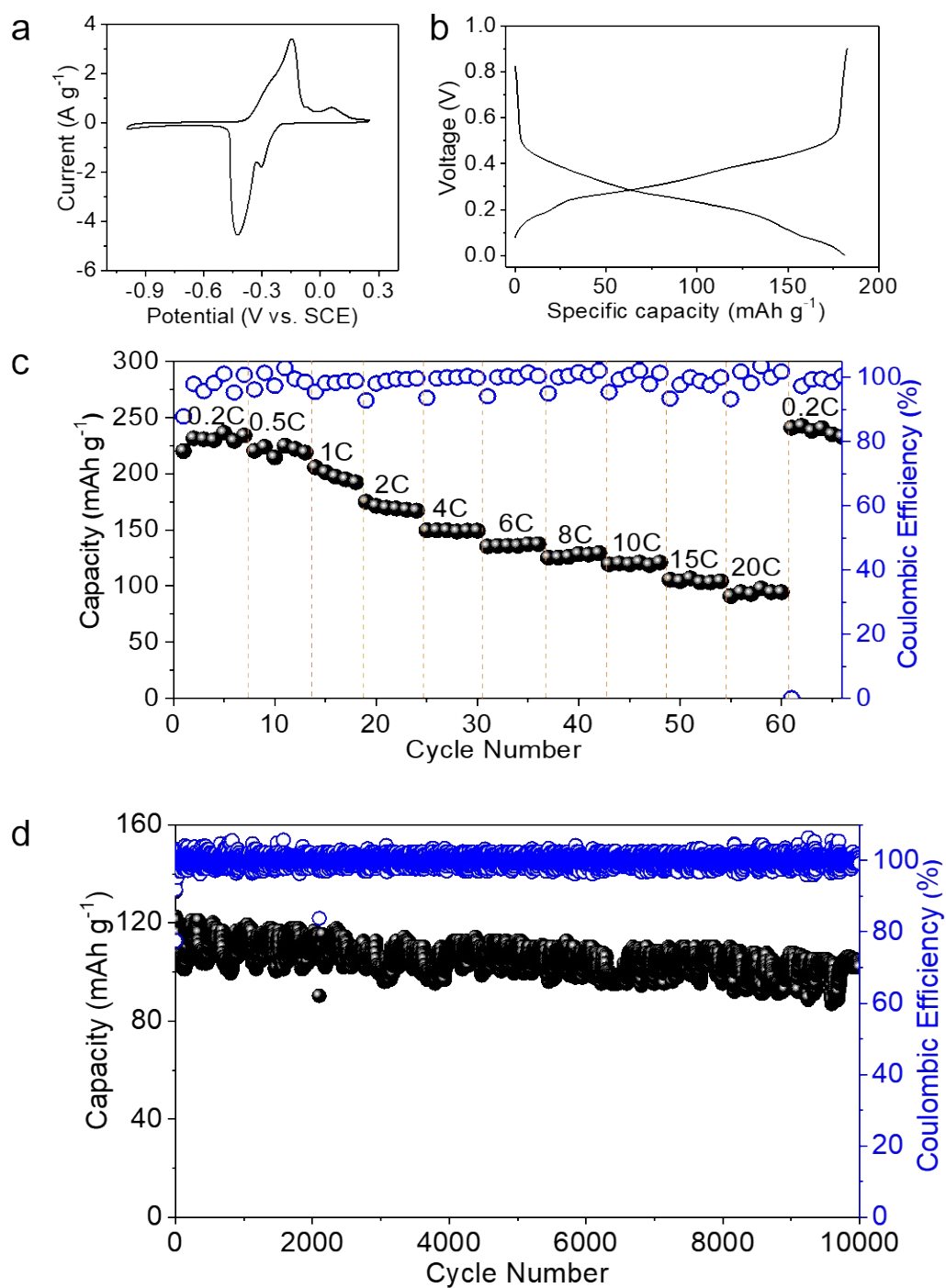


Fig. S35. Electrochemical performance of nPZ/KB anode vs. AC cathode in 2 M ZnSO₄ electrolyte. (a) CV curves at 1 mV s⁻¹. (b) Voltage profiles at 1 C. (c) Rate capabilities from 0.2 C to 20 C. (d) Capacity retention for 10,000 cycles at 10 C.

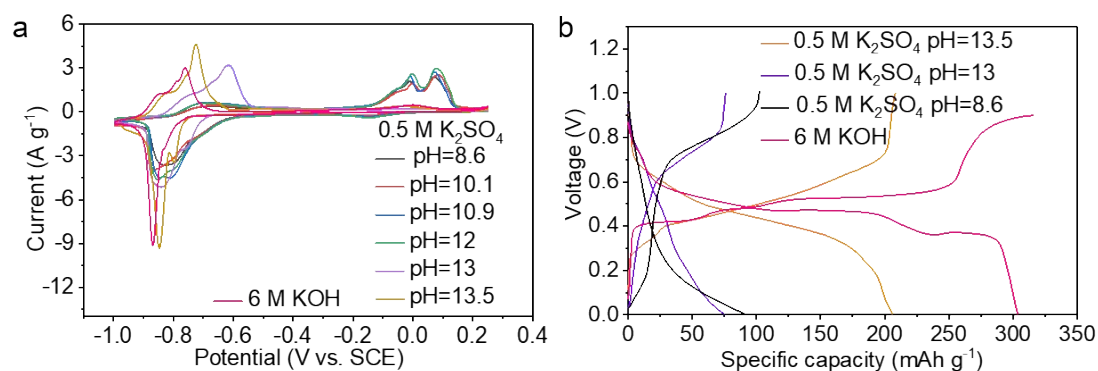


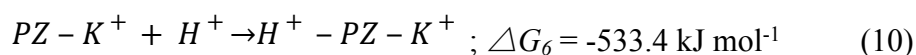
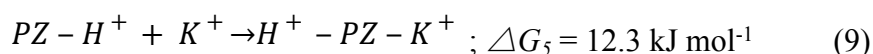
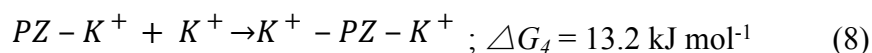
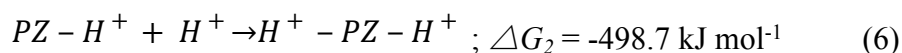
Fig. S36. (a) CV curves and (b) voltage profiles of nPZ/KB in aqueous electrolyte with different pH value.

The pH values of the electrolyte have significant influences on the electrochemical performances of the nPZ/KB anodes. We have thoroughly investigated the electrochemical performance of nPZ/KB anode in 0.5 M K₂SO₄ with various pH values (8.6, 10.1, 10.9, 12, 13, and 13.5), which was adjusted by adding different mass of 6 M KOH solutions. As shown in Fig. S36, when the pH was 8.6, the nPZ/KB anode presented a strong reduced peak at -0.83 V (*vs.* SCE) and a weak reduced peak at -0.15 V (*vs.* SCE). Correspondingly, it had a weak oxidized peak at -0.69 V (*vs.* SCE) and two overlapped oxidized peaks at -0.01 V and 0.07 V (*vs.* SCE). With the pH value increasing to 13.0, only one reduced peak at -0.84 V (*vs.* SCE) with a weak shoulder peak at -0.76 V (*vs.* SCE) were found, and the corresponding reversible oxidized peak at -0.62 V (*vs.* SCE) with a shoulder peak at -0.74 V (*vs.* SCE) occurred. It demonstrated

that the electrochemical energy storage mechanisms in the neutral electrolyte and alkaline electrolyte were different. As the pH value further increasing to 13.5, the nPZ/KB anode presented higher kinetic and smaller polarization. Similar phenomenon was also be seen in 6 M KOH electrolyte with high pH value. The performance changes of nPZ/KB anode in different pH value electrolytes might be attributed to the competitive adsorption reaction of H^+ and K^+ on the electronegative N atom in phenazine.

Furthermore, the DFT calculation results verified that the trace amounts of H^+ in the electrolyte could affect the electrochemical performance of phenazine anode. We showed the possible reaction process in Equation (5) to (10) and calculated the Gibbs free energy of every reaction step.

When the nPZ/KB anode was immersed into the aqueous K_2SO_4 electrolyte, the trace amounts of H^+ could coordinate with the electronegative N atom in phenazine spontaneously, due to the satisfactory Gibbs free energy ($\Delta G_1 = -533.4 \text{ kJ mol}^{-1}$ and $\Delta G_2 = -498.7 \text{ kJ mol}^{-1}$). However, the coordinated reaction of K^+ and N atom in phenazine was not easy to occur due to the small value of $\Delta G_3 (-7.7 \text{ kJ mol}^{-1})$ and the positive value of $\Delta G_4 (13.2 \text{ kJ mol}^{-1})$. Furthermore, we also investigated the possible intermediate reaction processes. As shown in Equation (9) and (10), PZ- H^+ could not coordinate with K^+ ($\Delta G_5 = 12.3 \text{ kJ mol}^{-1}$), while PZ- K^+ could coordinate with H^+ spontaneously ($\Delta G_6 = -533.4 \text{ kJ mol}^{-1}$).



PZ represented phenazine in the equations above; ΔG_5 represented the Gibbs free energy.

Through experimental results and thermodynamic calculations analysis above, we can conclude that:

(1) In the univalent K_2SO_4 electrolyte, the trace amounts of H^+ could coordinate with the active N atom in phenazine spontaneously, which was not beneficial for the electrochemical charge storage.

(2) When the pH value of the electrolyte was lower than 13, there are the competing coordinated reactions between K^+ and H^+ with the electronegative N during the electrochemical redox reactions.

(3) As the increase of pH value, the H^+ content decreases in the electrolyte solution. The coordinated reactions between H^+ and phenazine molecular is impeded, which

enables the phenazine anode delivers the better electrochemical performance in alkaline electrolyte.

Table S6. Technology comparison of potential batteries for utility applications^{12, 23}

Type ^[a]	open circuit voltage(V)	operating temperature (°C)	Discharge time	self-discharge % per month,20°C	cycle life (deep cycles)	round-trip DC energy efficiency(%)
LAB	2.1	-40-60	up to 8 h	4-50	1,000	50-75
NCB	1.35	-10-45	up to 4 h	5-20	2,000	55-70
VRB	1.4	10-40	4-12 h	3-9	5,000	65-80
LCB	2.1	-40-60	up to 4 h	-	3,000	-
Na-S	2.1	300-350	4-8 h	negligible	4,000	75-90
ZEBRA	2.6	300-350	4-8 h	negligible	3,000	75-90
C-CL	3-4	-25-40	up to 4 h	2	1,000	94-99
LT- LFP	1.7	-25-40	up to 4 h	2	4,000	94-99
PZ-NMO	0.8	-20-50	-	-	13,000	80
PZ-NiOOH	1.4	-40-30	-	-	100,000	95

^[a] LAB: lead-acid batteries, NCB: nickel-cadmium batteries, VBR: all-vanadium redox flow batteries, LCB: lead-carbon ultrabatteries, Na-S: sodium-sulfur batteries, ZEBRA:Zeolite Battery Research Africa, C-LC: Li-ion batteries of C anode and LiCoO₂ cathode, LT-LFP: Li-ion batteries of Li₄Ti₅O₁₂ anode and LiFePO₄ cathode, NZ-NMO: alkaline aqueous rechargeable batteries of phenazine anode, 10 M NaOH electrolyte and Na_{0.44}MnO₄ cathode, PZ-NiOOH: alkaline aqueous rechargeable batteries of phenazine anode, 6 M KOH electrolyte and NiOOH cathode.

References

1. D. S. Palmer, A. Llinàs, I. Morao, G. M. Day, J. M. Goodman, R. C. Glen and J. B. O. Mitchell, *Mol. Pharm.*, 2008, **5**, 266-279.
2. J. F. Kucharyson, L. Cheng, S. O. Tung, L. A. Curtiss and L. T. Thompson, *J. Mater. Chem. A*, 2017, **5**, 13700-13709.
3. A. Hollas, X. Wei, V. Murugesan, Z. Nie, B. Li, D. Reed, J. Liu, V. Sprenkle and W. Wang, *Nat. Energy*, 2018, **3**, 508-514.
4. W. Tang, X. Gao, Y. Zhu, Y. Yue, Y. Shi, Y. Wu and K. Zhu, *J. Mater. Chem.*, 2012, **22**, 20143-20145.
5. D. Sun, X. Xue, Y. Tang, Y. Jing, B. Huang, Y. Ren, Y. Yao, H. Wang and G. Cao, *ACS Appl. Mater. Interfaces*, 2015, **7**, 28337-28345.
6. D. Sun, G. Jin, Y. Tang, R. Zhang, X. Xue, X. Huang, H. Chu and H. Wang, *J. Electrochem. Soci.*, 2016, **163**, A1388-A1393.
7. Y. Liang, Y. Jing, S. Gheytani, K.-Y. Lee, P. Liu, A. Facchetti and Y. Yao, *Nat. Mater.*, 2017, **16**, 841-848.
8. W. Deng, Y. Shen, J. Qian and H. Yang, *Chem. Commun.*, 2015, **51**, 5097-5099.
9. X. Dong, L. Chen, J. Liu, S. Haller, Y. Wang and Y. Xia, *Sci. Adv.*, 2016, **2**, e1501038.
10. S. Gheytani, Y. Liang, F. Wu, Y. Jing, H. Dong, K. K. Rao, X. Chi, F. Fang and Y. Yao, *Adv. Sci.*, 2017, **4**, 1700465.
11. Q. Zhao, W. Huang, Z. Luo, L. Liu, Y. Lu, Y. Li, L. Li, J. Hu, H. Ma and J. Chen, *Sci. Adv.*, 2018, **4**, eaao1761.
12. T. Sun, C. Liu, J. Wang, Q. Nian, Y. Feng, Y. Zhang, Z. Tao and J. Chen, *Nano Research*, 2020, **3**, 508-514.

13. Q. Wang, Y. Liu and P. Chen, *J. Power Sources*, 2020, **468**, 228401.
14. K. Wozniak, B. Kariuki and W. Jones, *Acta Crystallographica Section C*, 1991, **47**, 1113-1114.
15. P. Hohenberg and W. Kohn, *Physical Review*, 1964, **136**, B864-B871.
16. W. Kohn and L. J. Sham, *Physical Review*, 1965, **140**, A1133-A1138.
17. J. Clark Stewart, D. Segall Matthew, J. Pickard Chris, J. Hasnip Phil, I. J. Probert Matt, K. Refson and C. Payne Mike, *Journal*, 2005, **220**, 567.
18. J. P. Perdew, K. Burke and M. Ernzerhof, *Phys. Rev. Lett.*, 1996, **77**, 3865-3868.
19. S. Grimme, *J. Comput. Chem.*, 2004, **25**, 1463-1473.
20. S. Grimme, *J. Comput. Chem.*, 2006, **27**, 1787-1799.
21. M. Lee, J. Hong, H. Kim, H.-D. Lim, S. B. Cho, K. Kang and C. B. Park, *Adv. Mater.*, 2014, **26**, 2558-2565.
22. R. S. Assary, F. R. Brushett and L. A. Curtiss, *RSC Advances*, 2014, **4**, 57442-57451.
23. Z. Yang, J. Zhang, M. C. W. Kintner-Meyer, X. Lu, D. Choi, J. P. Lemmon and J. Liu, *Chem. Rev.*, 2011, **111**, 3577-3613.